UNIVERSITY OF UTRECHT

INSTITUTE FOR THEORETICAL PHYSICS

Numerical Analysis of Electrokinetic Flow through a Cylindrical Channel with a Charge Regulation Boundary Condition

Author:
Dustin van Weersel BSc

Supervisors:
Dr. Sela Samin
Prof. Dr. René van Roij

December 15, 2016

Abstract

Electrokinetic flow, i.e. the combined pressure driven and electroosmotic flow, in charged micrometer sized channels is an important aspect of microfluidics. Numerical models describing this flow often employ a constant surface charge or constant electric potential boundary condition at the channel wall. This work proposes a model that uses an alternative boundary condition, based on a single chemical reaction, to describe the channel surface charge. The resulting streaming potential, axial velocity profiles and axial ion concentration profiles of this model are then compared to a constant surface charge model. We conclude that the model with the altered boundary condition produces similar values for the streaming potential and similar electrokinetic flow profiles when the applied electric field is weak. Also, the timescales needed for the electric potential and ion concentration profiles to reach equilibrium are consistent with the constant charge model. When the applied electric field is strong, and dominates the electrokinetic flow, a reduced axial velocity profile is found.

Contents

1   Introduction

Microfluidic devices, micrometer sized systems that process or manipulate small (10^{-9} to 10^{-18} L) amounts of fluids, are interesting theoretical systems with a multitude of practical applications. Moreover, the reduced size and low volume makes them promising alternatives for conventional laboratory set ups, with the added benefit of being very cost effective. Electrokinetic flow, i.e. the flow of an electrolyte solution through a narrow capillary due to the combined action of a pressure and potential gradient, is of great importance in microfluidic devices. In this context, charged micro- and nanochannels serve as interesting systems in understanding facets of electrokinetic transport such as electroosmosis, streaming potential, current density distributions and velocity profiles, while also providing a multitude of practical applications like separation of biomolecules [24, 37], detection [4], water desalination [18] and energy conversion [7, 40].

The theory of electrokinetic transport was first presented by Rice and Whitehead (1965) [30] and has since been greatly expanded on with the addition of several textbooks [9, 14, 22, 29] and numerous articles [5, 6, 16, 17, 20, 27, 28, 34, 41, 43, 44]. We note that these citations are just a small part of the body of work concerning electrokinetic transport. Most of the aforementioned studies only focus on steady state solutions of the governing equations.

Concurrently, developments in finite element method (FEM) software and increase in computing power allows for the simulation of the fully coupled pressure driven and electroosmotic flow with minimal technical knowledge and hardware requirements. This allows one to go far beyond this theoretical framework and study the full physical behaviour of the system. An example of this is the treatment of the flow of an electrolye in a charged cylindrical capillary by Masliyah and Bhattacharjee (2006) [22].

The theoretical system under consideration consists of a microchannel with radius a and length L_c and a surface charge density ρ_c connected to two reservoirs. Across the system a pressure gradient, due to an applied pressure at the entrance reservoir, and an electric potential gradient, due to an applied electric field at the exit reservoir, is applied. The system is filled with a symmetrical electrolyte solution, and the ions in the solution are modelled as monovalent point charges.

In this work, we will first derive analytical expressions for the electric potential, radial velocity distribution and the streaming potential in the case of an infinitely long channel and a low surface potential. Afterwards, we construct a model, employing the coupled Poisson, Nernst-Planck and Navier-Stokes equation, describing the combined pressure driven and electroosmotic flow in a finite charged cylindrical channel. We will make a comparison between the quantities obtained through this numerical model and the derived analytical expressions. Once we have validated the model, we present an alternative model, based on a simple charge regulating process at the channel wall. By considering this altered boundary condition, we hope to improve on the widely used constant surface charge boundary condition [6, 27, 28, 34, 43] at the channel wall.

2 Electrokinetic Theory

2.1 The System

We consider an axisymmetric system consisting of two cylindrical reservoirs connected by a cylindrical channel (Fig. 2.1). The reservoirs are considerably larger than the channel. The feed reservoir contains a symmetrical electrolyte (one anion and one cation, with valency z) with a constant concentration c_∞. The channel length L_c is assumed to be far greater than its radius a, which takes values between 50 nm and 5 μm. The channel surface carries a surface charge density of ρ_c, which manifests itself due to electrochemical reactions beteen the surface and the solution. The exit reservoir has an unspecified concentration of ions and zero hydrostatic pressure. At the entrance reservoir, we apply a pressure p_0. Furthermore, an electrode connects the two reservoirs such that a potential difference can be applied across the system, or equivalently an electric field E_x.
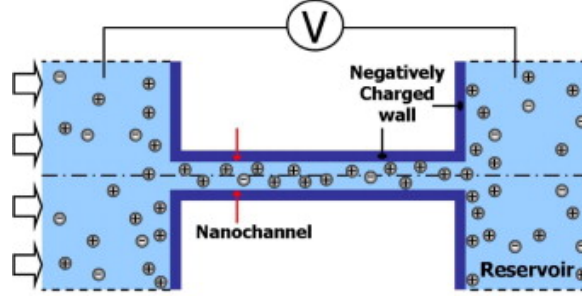

Figure 2.1: Choi and Kim (2009) [44] A schematic drawing of the considered system. The entrance reservoir is filled with a electrolyte solution which is pushed through the channel by a pressure p. An electrode connects the two reservoirs, applying a potential difference. The walls of the channel carry a negative charge.

2.2 Governing Equations

The saline solution is subject to two different forces. Firstly the hydrostatic pressure difference pushes the solution through the channel. Secondly, electroosmotic effects, due to the applied electric field and the electric double layer, mobilize the free charges in the solution. This interplay is described by the Nernst-Planck equation

$$-\frac{\partial n_i}{\partial t} = \nabla \cdot J_i = \nabla \cdot \left[n_i \boldsymbol{u} - D_i \nabla n_i - \frac{z_i e D_i n_i}{k_B T} \nabla \phi \right]. \tag{2.1}$$

Here, J_i is the molar flux of species i in ions/m^{2}s. n_i is the number concentration of species i (1/m^3), with D_i being its diffusivity in m^2/s. z_i is the ion valency and ϕ is the local electric potential (V). e is the elementary charge, k_B is the Boltzmann constant and T is the temperature in Kelvin. From this equation we see that the flux is determined by the number

concentration gradient, the changes in the local electric potential and the advection by the velocity field **u**. When looking for steady state solutions, $\partial_t n_i = 0$ and we obtain the steady state Nernst-Planck equation

$$\nabla \cdot J_i = 0. \tag{2.2}$$

The velocity field of the solution is described by the (incompressible) Stokes equation for momentum transfer

$$-\nabla p + \mu \nabla^2 \mathbf{u} - \rho_f \nabla \phi = 0, \tag{2.3}$$

$$\vec{\nabla} \cdot \boldsymbol{u} = 0. \tag{2.4}$$

Here the flow is assumed to be laminar (low Reynolds number), μ is the viscosity (Pa·s), and ρ_f the local free charge density (C/m^3). The electric potential is determined by the local free charge density ρ_f through the Poisson equation

$$\nabla^2 \phi = -\frac{\rho_f}{\varepsilon}. \tag{2.5}$$

with ε the permetivity of the solution (F/m).

2.3 The Electric Double Layer

Substances that come into contact with aqueous medium often develop an electric surface charge [9, 29]. This can be due to ionization of surface groups, adsorption of ions or other mechanisms [22]. This charged surface attracts the ions and repels the co-ions in the solution, giving rise to the so called electric double layer [10]. Due to thermal movement, the counterions that are attracted to the charged surface spread out and form a *diffuse* double (Fig. 2.2) layer [14] with charateric width λ_D.

The following analysis is largely derived from Rice and Whitehead (1965) [30]. The electric potential ϕ in the channel is assumed to be a linear combination of the applied external potential and the wall surface potential. If we assume that the potential due to the electric double layer is independent of axial position, which is valid for infinitely long channels, we can write

$$\phi(x,r) = \psi(r) + [\phi_0 - xE_0]. \tag{2.6}$$

Here, $\psi(r)$ is the electric potential due to the electric double layer at equilibrium without any flow or applied electric field. ϕ_0 is the imposed potential at $x = 0$, which we take to be zero, while $[\phi_0 - xE_0]$ is the electric potential at any location solely due to the application of an electric field E_0. For convenience, we consider the special case of a symmetric monovalent electrolyte ($z = z_+ = -z_-, z = 1$)

The Poisson Eq. 2.5 in cylindrical coordinates reads

$$\frac{1}{r}\frac{\partial}{\partial r}\left(r\frac{\partial \phi}{\partial r}\right) + \frac{\partial^2 \phi}{\partial x^2} = -\frac{\rho_f}{\varepsilon}. \tag{2.7}$$
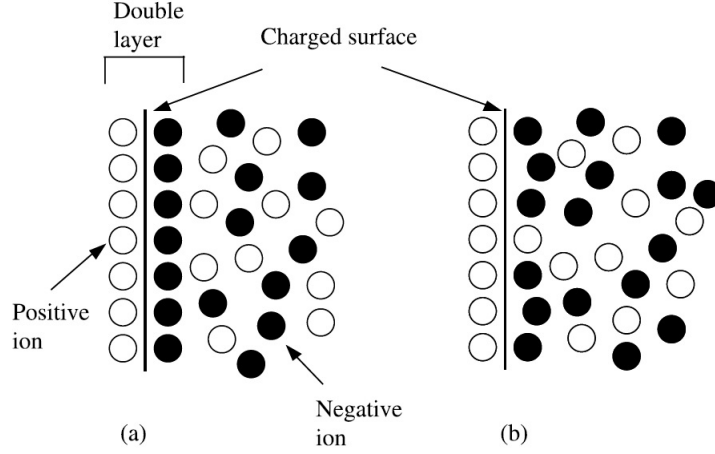
3

Figure 2.2: Masliyah and Bhattacharjee (2006) [22] The electric double layer (a) as envisioned by Helmholtz (b) the diffuse double layer

After inserting Eq. 2.6 we obtain

$$\frac{1}{r}\frac{d}{dr}\left(r\frac{d\psi}{dr}\right) = -\frac{\rho_f}{\varepsilon}. \tag{2.8}$$

where $r = 0$ is the axis of symmetry and $r = a$ is the channel wall. The space charge density of the free ions ρ_f can be written as the sum of the number concentration and their valencies.

$$\rho_f = \sum_{i=1}^{2} z_i e n_i. \tag{2.9}$$

Using the Boltzman distribution to express the number concentration n_i in terms of the electric potential ψ and the number concentration in the absence of an electric double layer n_∞ gives the Poisson-Boltzmann equation

$$\frac{1}{r}\frac{d}{dr}\left(r\frac{d\psi}{dr}\right) = -\frac{2zen_\infty}{\varepsilon}\sinh\left(\frac{ze\psi}{k_BT}\right). \tag{2.10}$$

If we also consider a low enough surface potential ($\psi \leq 25$ mV, or $e\psi/k_BT \leq 1$ for $z = 1$ [11]), we can use the Debye-Hückel approximation

$$\sinh\left(\frac{ze\psi}{k_BT}\right) \approx \frac{ze\psi}{k_BT}, \tag{2.11}$$

to obtain the linearised Poisson-Boltzmann equation

$$\frac{1}{r}\frac{d}{dr}\left(r\frac{d\psi}{dr}\right) = -\frac{2z^2e^2n_\infty}{\varepsilon k_BT}\psi = \kappa^2\psi, \tag{2.12}$$

where κ^{-1} is the Debye length, which is interpreted as a measure of the thickness of the electric double layer. With the boundary conditions being

$$r = h \implies \psi = \zeta,$$
$$r = 0 \implies \frac{d\psi}{dr} = 0,$$

the solution to Eq. 2.12 is

$$\psi = \zeta \frac{I_0(\kappa r)}{I_0(\kappa a)}, \tag{2.13}$$

with I_0 the zeroth-order modified Bessel function of the first kind. Concluding, the full potential is given by

$$\phi(x, r) = \zeta \frac{I_0(\kappa r)}{I_0(\kappa a)} + x E_0, \tag{2.14}$$

and the free charge density is

$$\rho_f = -\varepsilon \kappa^2 \zeta \frac{I_0(\kappa r)}{I_0(\kappa a)}. \tag{2.15}$$

2.4 Axial Velocity

In this section we deduce an analytical expression for the axial velocity to compare to numerical results. As a starting point we consider the axial component of the modified Stokes equation.

$$\mu \frac{1}{r} \frac{d}{dr} \left(r \frac{du_x}{dr} \right) = \frac{dp}{dx} + \rho_f \frac{d\phi}{dx} - \rho g_x \tag{2.16}$$

where u_x is the axial velocity, μ is the viscosity and ρ the mass density. g_x is the gravitational acceleration, which for a horizontal channel is zero, and p the pressure. Because we are considering fully developed flow $p_x = -dp/dx$ is a constant. Using this, $E_x = -\partial \phi / \partial x$, and Eq. 2.9 we obtain

$$\mu \frac{1}{r} \frac{d}{dr} \left(r \frac{du_x}{dr} \right) = -p_x + \varepsilon \kappa^2 \zeta E_x \frac{I_0(\kappa r)}{I_0(\kappa a)} \tag{2.17}$$

with the boundary conditions

$$r = a \implies u_x = 0, \tag{2.18}$$

$$r = 0 \implies \frac{du_x}{dr} = 0. \tag{2.19}$$

The first boundary condition specifies that the parallel velocity of the fluid at the channel wall is zero i.e. the no-slip boundary condition. The second condition is a symmetry condition on the flow, which is valid due to the symmetry in the system. The solution of Eq. 2.17 subject to the boundary conditions is given by

$$u_x(r) = \frac{a^2}{4\mu} \left[1 - \left(\frac{r}{a} \right)^2 \right] p_x - \frac{\varepsilon \xi}{\mu} \left[1 - \frac{I_0(\kappa r)}{I_0(\kappa a)} \right] E_x. \tag{2.20}$$

The first term is only dependent on the applied pressure gradient p_x and has a parabolic profile. It is normally referred to as the Poisseuille flow. The second term is proportional to the electric field E_x and describes the electroosmotic flow generated due to the applied electric field E_0. Fig. 2.3 shows the axial velocity profiles for pure dimensionless pressure driven flow (Eq. 2.21) and pure dimensionless electroosmotic flow (Eq. 2.22). The electroosmotic flow profile (Fig. 2.3(b)) becomes more constant throughout the channel as κa increases.

$$U_{x,p} = \frac{u_x}{a^2 p_x/2\mu} = 1 - \left(\frac{r}{a}\right)^2, \tag{2.21}$$

$$U_{x,E} = \frac{u_x}{-\varepsilon E_x \xi/\mu} = 1 - \frac{I_0(\kappa r)}{I_0(\kappa a)}. \tag{2.22}$$
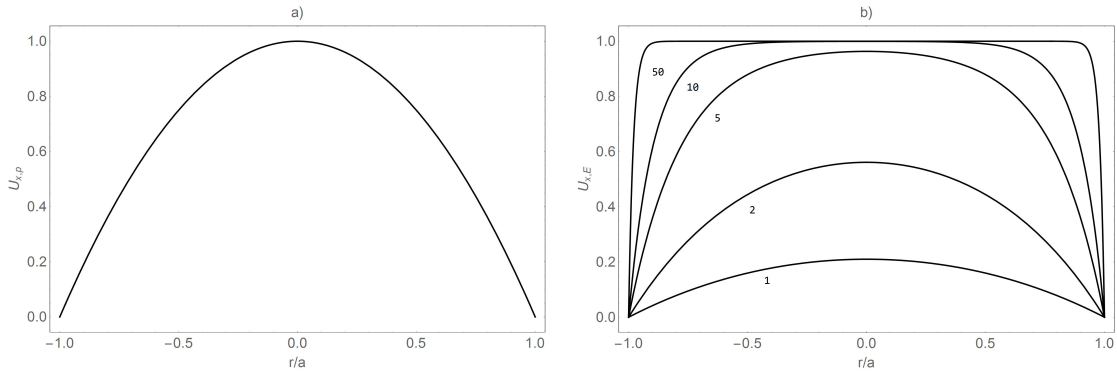

Figure 2.3: The dimensionless axial velocity profile for pure pressure driven flow (a) and purely electroosmotic flow for different values of the scaled channel width κa (b).

2.5 Streaming Potential

When we apply a pressure gradient to our system, the non-electroneutral double layer moves and induces a net current. As a reaction, a potential builds up across the pore to prevent a net current flow at steady state. This is called the *streaming potential* [30]. To deduce an analytical expression, we first look at the local current density vector (A/m^2). The local current density $\boldsymbol{i}$ is the sum of the individual fluxes of the ions in the solution

$$\boldsymbol{i} = e \sum_i z_i \boldsymbol{J}_i. \tag{2.23}$$

Using Eq. 2.1 we can write

$$\boldsymbol{i} = e\boldsymbol{u} \sum_i z_i n_i - e \sum_i D_i z_i \nabla n_i - \frac{e^2 \nabla \psi}{k_B T} \sum_i z_i^2 D_i n_i. \tag{2.24}$$

We now look at the total current I, given by

$$\frac{I}{2\pi} = \int_0^a i_x r\, dr, \tag{2.25}$$

6

with i_x given by Eq. 2.24. Evaluating this expression gives

$$\frac{I}{2\pi} = \int_0^a u_x \sum_i e z_i n_i r dr - e \int_0^a \sum_i \left(D_i z_i \frac{\partial n_i}{\partial x} \right) r dr - \frac{e^2}{k_B T} \int_0^a \frac{\partial \phi}{\partial x} \sum_i (z_i^2 D_i n_i) r dr. \quad (2.26)$$

Using Eq. 2.9 for the space charge density and writing $\partial \phi / \partial x = -E_x$ Eq. 2.26 becomes

$$\frac{I}{2\pi} = \int_0^a u_x \rho_f r dr + \frac{e^2}{k_B T} E_x \int_0^a \left(\sum_i z_i^2 D_i n_i \right) r dr. \quad (2.27)$$

For simplicity, we set $D_i = D$ and consider a symmetrical electrolyte ($z_+^2 = z_-^2 = z^2$). Using the Boltzmann distribution we also note that

$$\sum_i n_i = 2n_\infty \cosh\left(\frac{ze\psi}{k_B T} \right) \approx 2n_\infty \left[1 + \frac{1}{2} \left(\frac{ze\psi}{k_B T} \right)^2 \right], \quad (2.28)$$

where we used the Debye-Hückel approximation ($ze\psi/k_B T \ll 1$). Using this, Eq. 2.27 becomes

$$\frac{I}{2\pi} = \int_0^a u_x \rho_f r dr + \frac{2e^2 z^2 D n_\infty E_x}{k_B T} \int_0^a \left[1 + \frac{1}{2} \left(\frac{ze\psi}{k_B T} \right)^2 \right] r dr. \quad (2.29)$$

The first term, which is dependent on the velocity field u_x, represents the current due to convection whereas the second term represents the current due to migration. Recognising the electric conductivity

$$\sigma_\infty = \frac{2e^2 z^2 D n_\infty}{k_B T}, \quad (2.30)$$

and inserting Eq. 2.13 for the potential, we can write Eq. 2.29 as

$$I = 2\pi \int_0^a u_x \rho_f r dr + \pi a^2 \sigma^\infty E_x F_{cc}, \quad (2.31)$$

with

$$F_{cc} = 1 + \left(\frac{ze\zeta}{k_B T} \right)^2 \frac{1}{I_0^2(\kappa a)} \int_0^a I_0^2(\kappa r) r dr. \quad (2.32)$$

The term F_{cc} accounts for the non-electroneutrality of the solution near the wall. Earlier work, such as Rice and Whitehead (1965) [30] use $F_{cc} = 1$. However, F_{cc} can deviate significantly from unity, especially at higher potentials and for $\kappa a < 5$, as shown in Fig. 2.4.

Eq. 2.31 can be evaluated using the expressions for ρ_f and u_x in Equations 2.15 and 2.20 respectively. This gives

$$\begin{aligned} I &= -\frac{\varepsilon \zeta p_x A_c}{\mu} \left(1 - \frac{2A_1}{\kappa a} \right) - \mu E_x A_c \left(\frac{\varepsilon \zeta \kappa}{\mu} \right)^2 \left(1 - \frac{2A_1}{\kappa a} - A_1^2 \right) + E_x A_c \sigma^\infty F_{cc}, \\ &= A_c \sigma^\infty F_{cc} \left[1 - \frac{(\varepsilon \zeta \kappa)^2}{\mu \sigma^\infty F_{cc}} \left(1 - \frac{2A_1}{\kappa a} - A_1^2 \right) \right] E_x - \frac{\varepsilon \zeta A_c}{\mu} \left(1 - \frac{2A_1}{\kappa a} \right) p_x. \end{aligned} \quad (2.33)$$
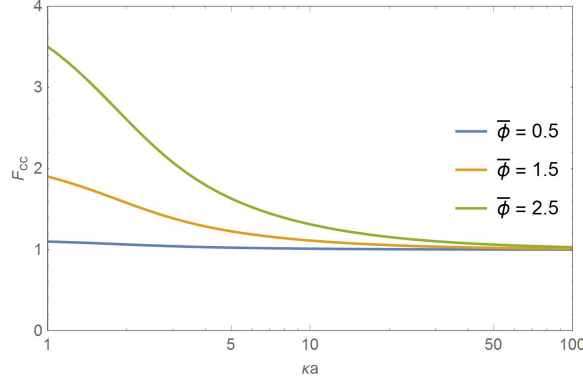
Figure 2.4: The value of F_{cc} given by Eq. 2.32 for different values of the dimensionless potential $\bar{\phi} = ze\zeta/k_B T$ and scaled radius κa. F_{cc} approaches unity for $\kappa a = 10$.

with the channel crossection area $A_c = \pi a^2$ and $A_1 = I_1(\kappa a)/I_0(\kappa a)$. Because we will be looking at steady state solutions, we set $I = 0$ to obtain

$$\left(\frac{E_x}{p_x}\right)_{I=0} = \frac{\varepsilon\zeta}{\mu\sigma^\infty}\left(1 - \frac{2A_1}{\kappa a}\right)f(\kappa a, \beta, F_{cc}), \tag{2.34}$$

with $\beta = \varepsilon^2\phi_c^2\kappa^2/\mu\sigma^\infty$ and

$$f(\kappa a, \beta, F_{cc}) = \frac{1}{F_{cc}\left(1 - \beta[1 - 2A_1/(\kappa a) - A_1^2]/F_{cc}\right)}. \tag{2.35}$$

Assuming a constant axial electric field E_x, we obtain

$$\Delta\psi = E_x L. \tag{2.36}$$

2.6 Slip Boundary Condition

In most fluid flow problems, a no-slip boundary condition is applied. However, in the case of micro, nano-channels and non-wetting surfaces, several studies [2, 31, 39, 46] suggest that this boundary condition might not be suitable.

The common alternative is the application of a linear slip boundary condition (Fig. 2.5). First proposed by Navier [26] and later by Maxwell [23], this boundary condition states that, at the liquid-solid interface, the parallel component of the velocity of the fluid, relative to the interface, is proportional to the shear rate at the surface:

$$u_x = b_s \boldsymbol{n} \cdot \left[\nabla\boldsymbol{u} + (\nabla\boldsymbol{u})^T\right] \cdot (1 - \boldsymbol{nn}) \cdot \boldsymbol{i}_x. \tag{2.37}$$

Or, in simpler form

$$u_x = b_s\left(\frac{\partial\boldsymbol{u}}{\partial r}\right)_{wall}, \tag{2.38}$$

where b_s is the slip length. This expression replaces the boundary condition in Eq. 2.18. This general boundary condition was explored, among others, by Yang and Kwok (2003) [16], Lauga (2007) [19], and Tandon and Kirby (2008) [38].
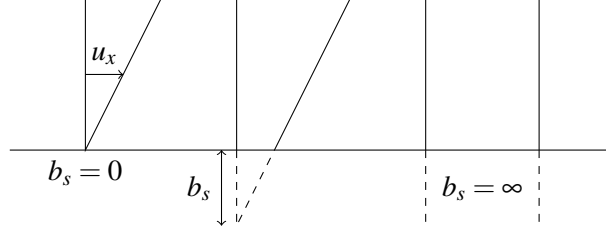

Figure 2.5: A schematic depiction of the Navier slip boundary condition. The parallel velocity is extrapolated linearly to zero behind the interface. The resulting length is the slip length b_s.

The solution to Eq. 2.17 with the slip boundary condition is

$$u_x(r) = \frac{a^2}{4\mu}\left[1 - \left(\frac{r}{a}\right)^2 + \frac{2b_s}{a}\right]p_x - \frac{\varepsilon\xi}{\mu}\left[1 - \frac{I_0(\kappa r)}{I_0(\kappa a)} - \kappa b_s\frac{I_1(\kappa a)}{I_0(\kappa a)}\right]E_x. \tag{2.39}$$

2.7 Charge Regulation

The basis for the existence of the EDL is the electric surface charge of the boundary. Often, a constant zeta potential [27, 43] or surface charge density [6, 28, 34] is used as a boundary condition for the surface. However, it is known from theory and experiments [1, 8, 32, 36] that the surface charge is dependent on the pH, salt concentration and the extent of the double-layer overlap because of the interactions of the ions with the channel surface.

Proposed alternatives are the Stern layer capacitance model [1, 40, 41] and the site-dissosciation-binding model [12, 33, 35, 36]. In this thesis we employ a simple 1-pK model [21, 42].

We assume that the surface charge is assumed to be entirely localized on the surface and stems from a concentration of ionized surface groups. Without loss of generality we consider the ionization of a generic group S due to the absorption of OH^-

$$SOH^- \rightleftharpoons S + OH^-. \tag{2.40}$$

The mass action law at equilibrium for this reaction states

$$10^{-pK} = \frac{[S][OH^-]}{[SOH^-]}, \tag{2.41}$$

where, for example [S] denotes the concentration of species S and pK is a constant that depends on the reaction. Using Eq. 2.40 we can rewrite Eq. 2.41 in terms of the ionized group SO^-

$$[SOH^-] = \frac{[S]}{\frac{10^{-pK}}{[OH^-]_0} + 1}. \tag{2.42}$$

Denoting the number of surface groups [S] by Γ, we can express the surface charge density ρ_c as a function of the material constants pK and Γ and the local ion concentration $[\mathrm{OH}]^-$

$$\rho_c = -e \frac{\Gamma}{\frac{10^{-\mathrm{pK}}}{[\mathrm{OH}^-]} + 1}. \tag{2.43}$$

3 Modelling Approach

The finite element method (FEM) [3,45] is a powerful tool in the computation of highly complex solutions to coupled partial differential equations (PDE) describing physical systems. By subdividing a continuous domain into a set of discrete sub-domains, called elements, and with enough computing power, approximate solutions to coupled PDE's can be found. In this thesis, we use the finite element method provided by Comsol Multiphysics software.

3.1 Geometry

The 3D system was modelled as a fully axisymmetrical geometry with axial coordinate x and radial coordinate r. The entrance and exit reservoir were built using two squares with length b. The channel consists of a rectangle with height a and length L_c (Figure 3.1).
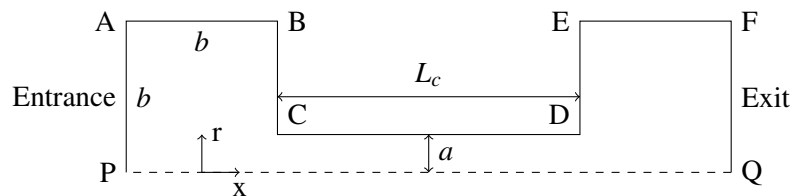

Figure 3.1: A schematic drawing of the geometry. The dashed line PQ represents the axis of symmetry

The Electrostatics, Laminar Flow and Transport of Diluted Species interfaces of COMSOL were employed to couple the Poisson-Boltzmann (Eq. 2.5), Navier-Stokes (Eq. 2.3) and Nernst-Planck equation (Eq. 2.1) respectively.

3.1.1 Poisson Equation

The electrostatics interface is a part of the AC/DC module in Comsol Multiphysics and is used to calculate the electrostatic potential in the system. We specified the solvent relative permettivity ε_r according to Table 4.1 and a space charge density of $Q = eN_A \cdot (c_1 - c_2)$ (C/m^3) on the entire domain. On the boundaries AB, EF and FQ (Fig. 3.1) the 'Zero Charge' ($\boldsymbol{n} \cdot \boldsymbol{D} = 0$) boundary condition was specified. The potential was set to 0 at AP, grounding the system. The sidewalls BC and DE carry a surface charge density of ρ_{sw} (C/m^2). The channel wall CD carries a surface charge density of ρ_c which at first is taken to be constant, but is later determined through a charge regulation scheme. A schematic overview of the relevant boundary conditions is presented in Fig 3.2.
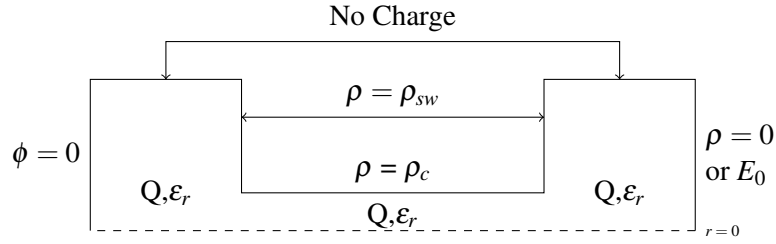
Figure 3.2: The boundary conditions for the Poisson equation. The entrance is grounded ($\phi = 0$), whereas the exit either carries zero charge or has an applied electric field E_0. The channel side walls carry a charge density ρ_{sw}, and the channel carries a charge density ρ_c. The interior is filled with a fluid with relative permetivity ε_r and charge Q. The boundaries representing the reservoir interior carry no charge.

3.1.2 Navier-Stokes Equation

The laminar flow interface provides the options needed for Comsol Multiphysics to calculate the velocity field $\boldsymbol{u}$ (m/s) and the local pressure p (Pa). The flow was set to be incompressible and non-turbulent and the density ρ (kg/m^3) and dynamic viscosity μ (Pa·s) were set to the values given by Table 4.1. On the sidewalls BC and ED (Fig. 3.1), the no-slip boundary condition was specified while BC, CD and DE satisfied the linear slip condition (Figure 3.3). In the case of zero slip length $b_s = 0$, the no-slip boundary condition was recovered. A pressure of p_0 (Pa) on the inlet PA and a zero pressure on the outlet FQ was applied. On the entire domain, the ions experience a Lorentz force of $Q \cdot \boldsymbol{E}$ (N/m^3). Intitally the pressure and velocity were taken to be zero. A schematic overview of the relevant boundary conditions is presented in Fig 3.3.
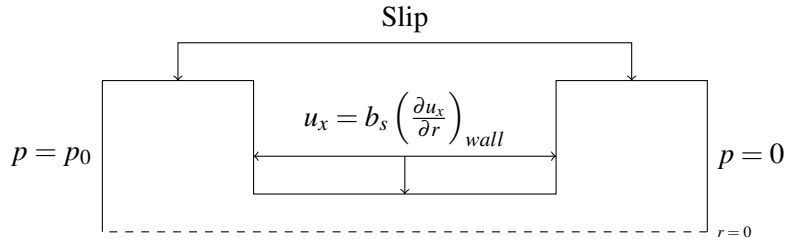

Figure 3.3: The boundary conditions for the Navier-Stokes equation. There is an applied pressure of p_0 on the entrance of the system, whereas the exit experiences zero pressure. The walls representing the interiors of the reservoirs have full slip ($b_s = \infty$), whereas the channel and the sidewalls have either a no slip or a partial slip boundary condition.

3.1.3 Nernst-Planck Equation

The movement of the ions in the solution are handled by the Transport of Diluted Species interface. In the Nernst-Planck equation, convection and migration terms were included and the existence of two ion species (c_1 and c_2), with valency -1 and 1 respectively, were

specified. The velocity field, given by the Laminar Flow Interface, as well as the electric potential, determined by the Electrostatics Interface, were given as input. The temperature T, the diffusion coëfficients $D_i = D$ (m^2/s) and charge coëfficients z_i were set to the values given by Table 4.1. On the boundary AB, BC, CD, DE and EF (Fig. 3.1) a no-flux ($-\boldsymbol{n} \cdot \boldsymbol{c}_i = 0$) boundary condition was applied. The concentration of the ion species c_1 and c_2 (mol/m^3) at the inlet PA was set to the constant value c_∞. For the outlet FQ, some situations demanded a constant concentration of the ion species, similar to the condition on AP. In other cases, the concentration was not specified and an outflowing boundary condition ($-\boldsymbol{n} \cdot D\nabla c_i = 0$) was applied. A schematic overview of the relevant boundary conditions is presented in Fig 3.4.
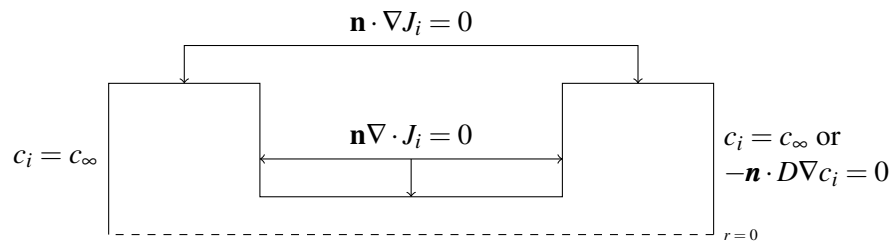

Figure 3.4: The boundary conditions for the Nernst-Planck equation. The inlet has a fixed concentration of $c_i = c_\infty$. The outlet either has the same fixed concentration, or an outflowing boundary condition of $--\boldsymbol{n} \cdot D\nabla c_i = 0$. There is no flux through any of the other walls.

3.2 Meshing

To employ the finite element method, an appropriate mesh needs to be created for the system. If the mesh is too coarse, the FEM fails to find a suitable approximate solution. When the mesh is too fine, the program uses a significant amount of computing power and a long time to find a solution. Ideally, our mesh is just fine enough to arrive at a solution.

We divide our system into two domains. One subdomain consists of the first four Debye lengths near the channel wall, which was implemented as a Mesh Control Domain. Here, the minimimum element size was set to $\lambda_D/6$ and the maximum element size was set to $\lambda_D/4$. For a concentration of, for example, $c_\infty = 1 \times 10^{-5}$ M, the resulting element size was between 0.16nm and 0.24nm. This resulted in a mesh of at least 4 elements (radially) per Debye length, ensuring ample resolution for the electric double layer. For the rest of the geometry, the mesh was calibrated for fluid dynamics and set to *Exta fine*, resulting in element sizes ranging from 0.24 nm to 30 nm. The mesh was then created using the built in options of Comsol Multiphysics, covering the entire domain in triangular elements. Fig. 3.5 shows the entire meshed geometry and the entrance of the channel.
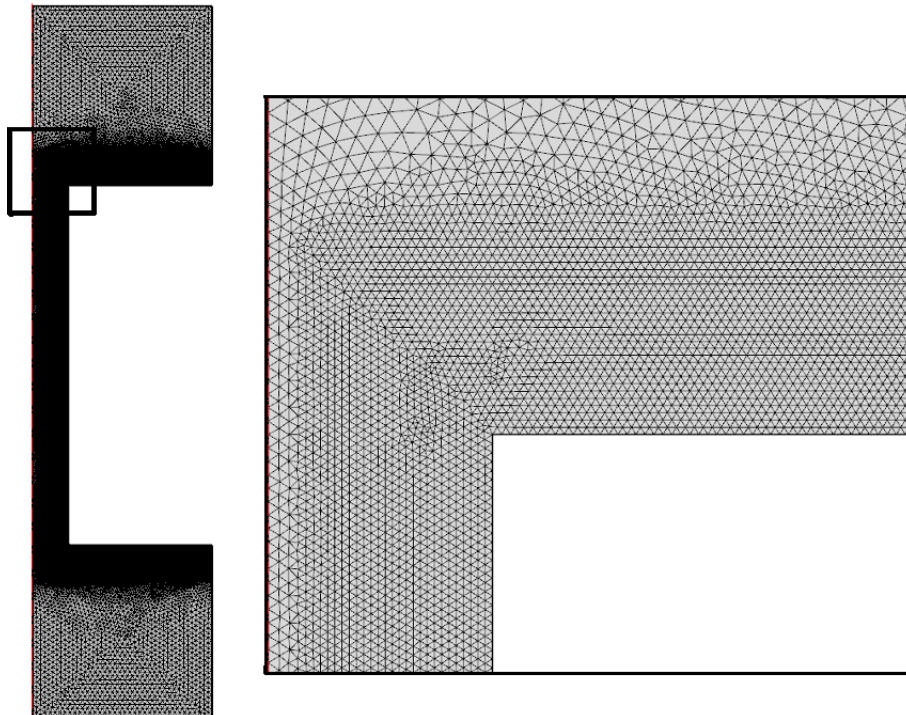
Figure 3.5: A screenshot of the entire meshed geometry and a zoomed in picture, generated by Comsol Multiphysics, for $\kappa a = 5$ and $L_c = 10a$. The more densely meshed area represents the first four Debye lengths near the wall.

4 Results and Discussion

In this section we will discuss the results obtained from the numerical simulation of a combined pressure and electric potential gradient driven flow through a system consisting of two reservoirs and a micro/nanochannel. We will first compare the non-charge regulating model with the theoretical results derived in section 2. We will also analyse the various assumptions made to derive these expressions, and how they pertain to the simulation. Afterwards, we explore the effects of changing certain physical parameters, like the bulk salt concentration c_∞, the applied pressure p_0, the capillary radius a and the slip length b_s. Finally, we visit the charge regulating model and compare it to the non charge regulating model.

Parameter	Value/Range
Relative solvent permetivity, ε_r	78.54
Bulk electrolyte concentration, c_∞	10^{-3}- 10^{-5} M
Ion diffusivity, D	10^{-9} m^2/s
Temperature, T	298 K
Fluid mass density, ρ	1000 kg/m^3
Fluid viscosity, μ	0.001 Pa·s
Applied pressure gradient, p_x	$1 \times 10^7 - 1 \times 10^8$ Pa/m
Capillary radius, a	50 - 500 nm

Table 4.1: Parameters used in the model.

The model in question was built according to the specifications outlined in Section 3 and represents a cylindrical, charged channel connected to two cylindrical reservoirs, filled with a symmetrical electrolyte solution as shown in Fig. 2.1. The boundaries AP, AB, EF and FQ represent regions where bulk conditions, unperturbed by the channel, apply. Consequently, they are taken to be uncharged, as they represent interiors. Furthermore, we apply a slip boundary condition ($b_s = \infty$) on AB and EF. The walls of the reservoirs are also incorporated in the model (BC and DE) and can carry appropriate surface charge densities or be considered electrically neutral. The channel wall CD carries a surface charge density of ρ_c, which can be taken to be constant, or determined through the charge regulation scheme (2.7).

Throughout this section we consider the transport of a symmetrical electrolyte solution, with bulk concentration c_∞ and diffusivity $D_i = D$, through our system. The solution is subject to forces as a result of an applied pressure gradient (pressure driven flow), an applied external electric field (electroosmotic flow) or both. The radius and depth of the reservoir b are taken to be to be 5 times the channel radius a to justify bulk conditions at AP, AB, EF and FQ. The channel length L_c was taken to be at least 10 times a. The potential at AP was set to zero, grounding the system. The values of several parameters used in the model are shown in Table 4.1. The Debye length λ_D was determined used Eq. 2.12 and took values between 50 and 500 nm. Some variables are referenced in their dimensionless form for convenience. Table 4.2 outlines these variables.

Variable	Expression
x-coordinate, $\bar{x}$	$\frac{x}{L}$
r-coordinate, $\bar{r}$	$\frac{r}{a}$
Surface charge density, $\bar{\rho}_c$	$\frac{ze}{\varepsilon k_B T \kappa}\rho_c$
Electric potential, $\bar{\phi}$	$\frac{ze}{k_B T}\phi$
Electric field, $\bar{E}$	$\frac{ze}{k_B T \kappa}E$
Pressure, $\bar{p}$	$\frac{z^2 e^2}{\varepsilon k_B^2 T^2 \kappa^2}p$
Velocity, $\bar{u}$	$\frac{u}{\kappa D}$

Table 4.2: The dimensionless form of some key variables referenced throughout this section

4.1 Validation

Before considering the charge regulating model, we need to check whether the simple non charge regulating model produces physical results. For this, we have derived analytical expressions for some key variables like the streaming potential and axial velocity in Section 2. Furthermore, we will aim to recreate the results presented in Chapter 14 of *Electrokinetic and Colloid Transport Phenomena* [22].

Most of the numerical validation used a channel radius such that $\kappa a = 5$, meaning the radius of the channel was 5 times the Debye length, and a bulk salt concentration of $c_\infty = 10^{-5}$ M. This implies a Debye length of roughly 100 nm and thus a channel radius of $a = 500$ nm. The channel surface was either taken to carry a constant surface charge of $\bar{\rho}_c = -1.15$ (roughly -0.2 mC^2/m) or a constant surface potential of $\bar{\phi}_c = -1$.

4.1.1 Pressure Driven Flow

As described in Section 2.5, when we apply a pressure gradient p_x, a potential sets up as a reaction to the flow of the non-electroneutral double layer. In this section we simulate this streaming potential and strive to emulate the results obtained from the analytical approach in Section 2.5. We also consider the various assumptions made in this section and how they affect the simulation results.

4.1.1.1 Boundary and Initial Conditions
The derived analytical expressions in Section 2.5 assume no axial variation in the concentration, and thus do not consider ion rejection by the channel due to the obstructing force exerted by the negatively charged channel wall. Accordingly, at both AP and FQ, the concentration was set to be c_∞. Eq. 2.20 and 2.34 are formulated using the channel electric potential, and thus we apply a constant potential of $\bar{\phi}_c = -1$ ($\phi \approx 0.025V$) on the channel wall. The simulation was run for $\kappa a = 1 - 9$ and a pressure gradient of $p_x = 1 \times 10^7$ Pa/m. An overview of the relevant boundary conditions is given in Table 4.3.

Boundary	Poisson	Nernst-Planck	Navier-Stokes
PQ	Axial symmetry	Axial symmetry	Axial symmetry
AB, EF	No charge	No Flux	Full slip
BC, DE	No charge	No Flux	No slip
CD	Constant potential, $\bar{\phi}_c$	No Flux	No slip
AP	$V = 0$	$c_i = c_\infty$	Pressure p_0
FQ	No charge	$c_i = c_\infty$	Zero pressure

Table 4.3: A summary of the boundary conditions of the governing equations, used in the analysis of the streaming potential at steady state.

17

4.1.1.2 Comparison to Analytical Results We will first dicuss the approximations made in Section 2 and what implications they have. It was assumed that our channel is infinitely long, neglecting any entrance/exit effects and axial concentration gradients, and that the linearisation of the Poisson-Boltzzmann equation holds. The midsection ($x = 0.5$) is furthest removed from the extrance and exit and thus we expect conditions there to be the most similar to the ones used in the theoretical analysis.
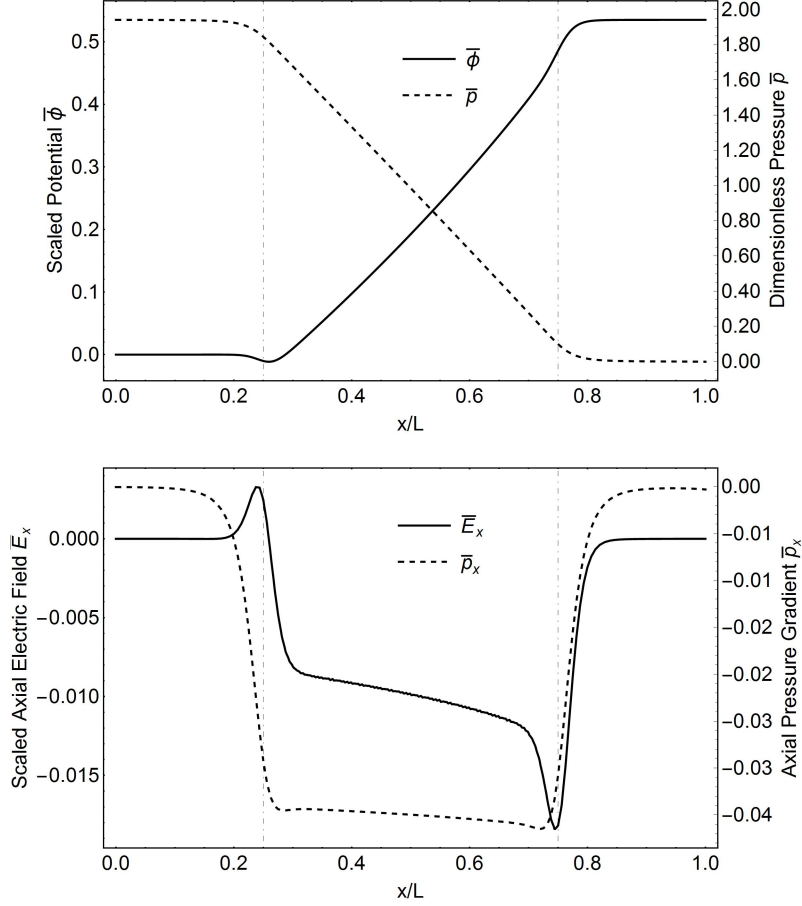

Figure 4.1: (a) The scaled electric potential $\bar{\phi}$ and the pressure with the corresponding scaled axial electric field $\bar{E}_x$ and scaled axial pressure gradënt p_x (b) along the axis of symmetry obtained by solving the governing equations. The solid lines represent the electric potential and field, while the dashed lines represent the pressure and pressure gradient. The simulation was run for $\kappa a = 5$ with a pressure gradient of 1×10^7 Pa/m and constant surface potential of $\bar{\phi}_c = -1$ on the channel wall. The vertical lines represent the entrance and exit of the channel.

Fig. 4.1a shows the electric potential and pressure along the symmetry axis PQ for $\kappa a = 5$, $\bar{\phi}_c$ = -1 and $p_x = 1 \times 10^7$ Pa/m. The values of $\bar{x} = 0.25$ and $\bar{x} = 0.75$ correspond to the entrance and exit, respectively, of the channel. We see that both variables are roughly constant in the reservoirs and we see marked variations at the entrance and exit, as we should expect.

Inside the channel, the electric potential has a non-linear decrease whereas the pressure drops off linearly. This is more clearly depicted in Fig. 4.1b which shows the axial electric field $\bar{E}_x = -\partial \bar{\phi}/\partial x$ and pressure gradient $\bar{p}_x = -\partial \bar{p}/\partial x$.

We will now compare the results for the axial velocity profile to the analytical expressions derived in 2. Firstly, we look at the axial component of the velocity, given by Eq. 2.20.

$$u_x = \frac{a^2}{4\mu} \left[1 - \left(\frac{r}{a} \right)^2 \right] p_x - \frac{\varepsilon\zeta}{\mu} \left[1 - \frac{I_0(\kappa r)}{I_0(\kappa a)} \right] E_0, \tag{4.1}$$

where ζ is the zeta potential, which we take to be equal to the potential on the channel wall. Furthermore, $p_x = -\partial p/\partial x$ and E_x are the axial pressure gradient and axial electrical field respectively measured at the capillary midsection. Fig. 4.2 shows the comparison of the measured axial velocity and the analytical expression for $\kappa a = 1, 5$ and 9. For all three values of κa, the analytic and measured values match extremely well.
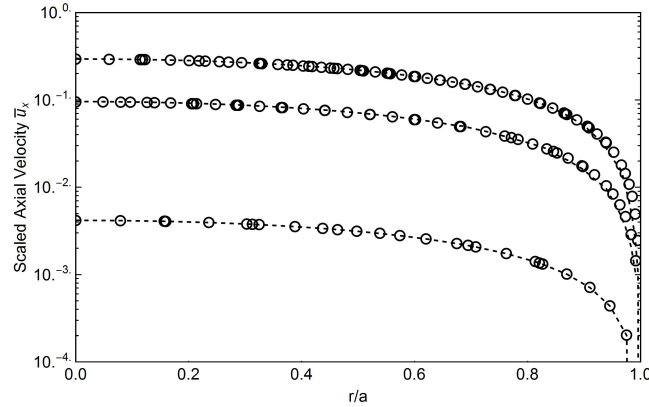

Figure 4.2: A comparison of the scaled axial velocity profile at the midsection of the channel, obtained through the numerical simulation, with the prediction given by the expression 4.1 for $\kappa a = 1, 5$ and 9.

Next up, we take a look at the streaming potential. Masliyah and Bhattacharjee (2006) [22] calculated the streaming potential by first evaluating the expression for the axial component of the electric field divided by the pressure gradient (Eq. 2.34) and then determining the streaming potential using $\Delta\phi = E_x L$. The values used for p_x and E_x are calculated by taking their respective values in the entrance and exit reservoir, and then dividing by their seperation. This calculation scheme assumes that the axial component of the electric field and the pressure are linear throughout the system. From Fig. 4.1 we already know this is not the case for the axial electric field. Fig. 4.3 shows the values of the streaming potential and the values obtained using the calculation scheme for various channel lengths. It is clear that the values, for $L_c = 50\lambda$, are in good agreement. For shorter and longer channels, however, the discrepancies between the analytic and measured values become larger.

It is worthwhile to look at the implications of the fixed concentration on the boundary FQ. When we substitute this condition for a convective flux boundary condition, as we will in
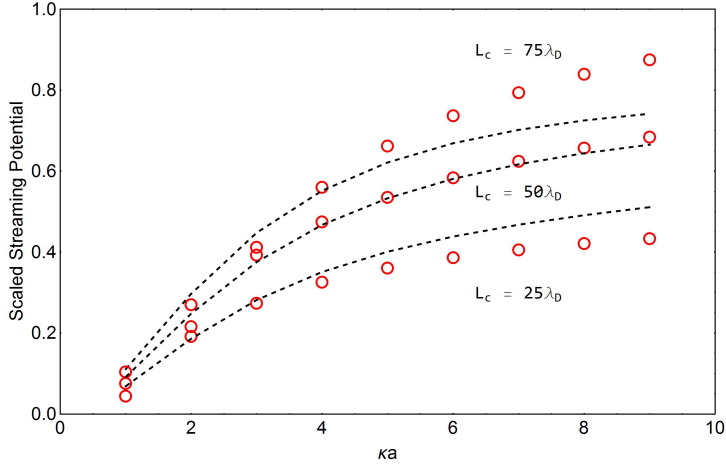
Figure 4.3: A comparison of the scaled streaming potential obtained from the numerical simulation and the prediction given by the calculation scheme of Masliyah and Bhattacharjee (2006) [22] for different values of the scaled channel radius κa and channel lengths L_c.

the coming sections, the concentration in the exit reservoir will no longer match the concentration in the entrance reservoir. Fig. 4.4 depicts the ion concentration profile and the electric potential along the axis ($r = 0$) of the channel for both boundary conditions. Fig. 4.4(a) shows that the axial variation of the concentration is greatly affected by changing the boundary condition. The electric potential along the axis (Fig. 4.4(b)) is nearly identical in the entrance reservoir and channel, and slightly higher in the exit reservoir for the convective flux boundary condition.
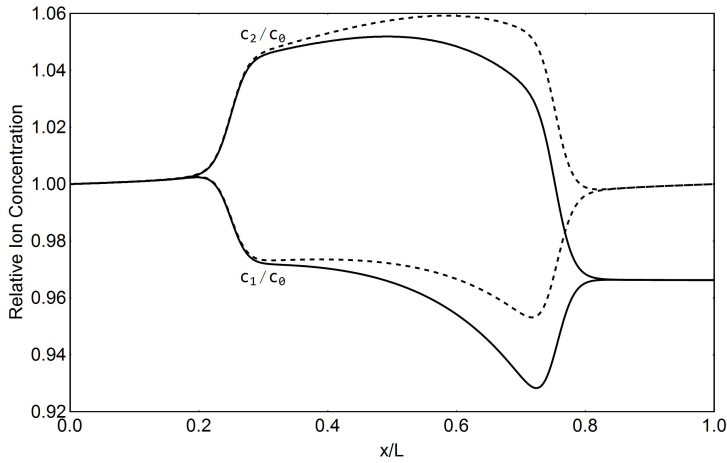

Figure 4.4: The axial concentration profiles of the relative concentrations c_i/c_∞ for $\kappa a = 5$ and $p_x = 1 \times 10^7$ Pa/m. The concentration stays relatively constant in the reservoirs ($x \leq 0.25$ and $x \geq 0.75$), whereas the negatively charged channel wall partially rejects ions entering the channel.

20

4.1.1.3 Velocity Profiles for Pressure Driven Flow with a Finite Slip Length

As discussed in section 2.6, the commonly used no-slip boundary condition on the channel is not always applicable. Here, we look into the effect of specifying a non-zero slip length b_s. The simulation was run for $b_s = 0, 25, 50, 75$ and 100 nm, with $p_x = 1 \times 10^7$ and 1×10^8 Pa/m. The scaled channel radius κa was set to 5.

Fig. 4.5 shows the numerical results together with the analytical curve given by Eq. 2.39. We see that, due to the non-finite slip length, the axial velocity at the wall ($r/a = 1$) is non-zero. Moreover, the entire profile seems to be shifted by a constant factor. The analytic curve seems to match reasonably well with the simulated values.
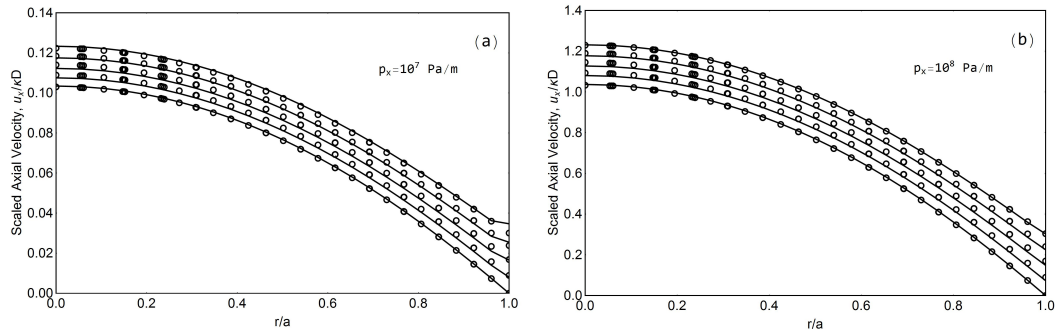

Figure 4.5: The axial velocity profile, $\bar{u}_x = u_x / \kappa D$, measured at the midsection ($\bar{x} = 0.5$) for various values of the slip length b_s and pressure gradient $p_x = 10^7$ (a) and 10^8 Pa/m, compared to the analytical expression 2.39.

It is clear that a finite slip length has a significant effect on the axial velocity in the channel. Due to this increased flow, especially near the wall, we also expect a higher streaming potential. Fig. 4.6 depicts the streaming potential for $p_x = 1 \times 10^7$ and 1×10^8 Pa/m. We see that our expectation is correct, and that the streaming potential increases linearly. Moreover, this effect is enhanced at higher pressures.
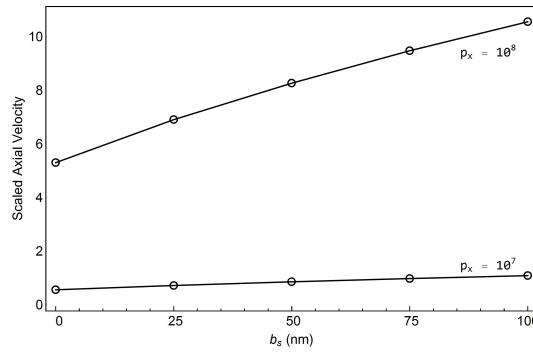

Figure 4.6: The scaled streaming potential for different values of the slip length b_s, with $\kappa a = 5$ and $p_x = 1 \times 10^7$ and 1×10^8 Pa/m. As we can see, the streaming potential increases linearly with the slip length.

21

4.1.2 Time Evolution of Electrolye Transport in a Microchannel

We now consider the dynamical behaviour of our system. Particularly, we are interested in the time scales needed for equilibrium to set up. Electrokinetic studies [17, 25] predict that the streaming potential sets up within the time scale of the hydrodynamic relaxation whereas simulations involving the extended Nernst-Planck equation [20] predict a time scale in the order of the ion diffusion.

4.1.2.1 Boundary and Initial Conditions It is known that, when the channel width a is in the order of the Debye length, there is significant ion rejection [5, 22]. Consequently, we set an outflowing boundary condition $(-\boldsymbol{n} \cdot \nabla c_i =)$ on the boundary FQ, as opposed to fixing the concentration. The time dependent governing equations were used to determine the evolution of the streaming potential and ion concentration distribution. The initial condition $(\tau = 0)$ was determined by solving the model without considering an applied pressure gradient. A summary of the boundary conditions is given in table 4.4.

Boundary	Poisson	Nernst-Planck	Navier-Stokes
PQ	Axial symmetry	Axial symmetry	Axial symmetry
AB, EF	No charge	$\boldsymbol{n} \cdot \boldsymbol{J}_i = 0$	Full slip
BC, DE	No charge	$\boldsymbol{n} \cdot \boldsymbol{J}_i = 0$	No slip
CD	Constant charge density, ρ_c	$\boldsymbol{n} \cdot \boldsymbol{J}_i = 0$	No slip
AP	$V = 0$	$c_i = c_\infty$	Pressure p_0
FQ	No charge	$-\boldsymbol{n} \cdot \nabla c_i = 0$	Zero pressure

Table 4.4: A summary of the boundary conditions of the governing equations, used in the analysis of the time evolution of the electrokinetic flow.

4.1.2.2 Simulation Results   We ran the simulation for $\kappa a = 5$ and with a constant surface charge density $\bar{\rho}_c$ of -1.15 ($\rho_c = 0.2$ mC/m^2). The geometry and parameters, apart from the outflowing boundary condition, are identical to the previous case. The output of the simulation was stored for various values of $\tau = \kappa^2 Dt$, ranging from 0.1 to 10.000. The results are shown in 4.7. In these plots, the dashed line represents the steady-state solution obtained using the time independent equations.

The graphs on the left side represent the potential and ion concentration within the first milisecond ($\tau \leq 10$, i.e. $t \leq 0.1 ms$), whereas the right side represents times up to $\tau = 10.000$, which equates to the first second. We can see that the potential sets up very rapidly, approaching the steady state value within 0.1 milisecond. The relative ion concentrations take significantly longer to equilibrate. For $\tau \leq 10$ the ion concentration does not seem to react, and even after $\tau = 10.000$ the relative ion concentration has not come within 5% of the steady state value. These observations are consistent with Masliyah (2006) [22].
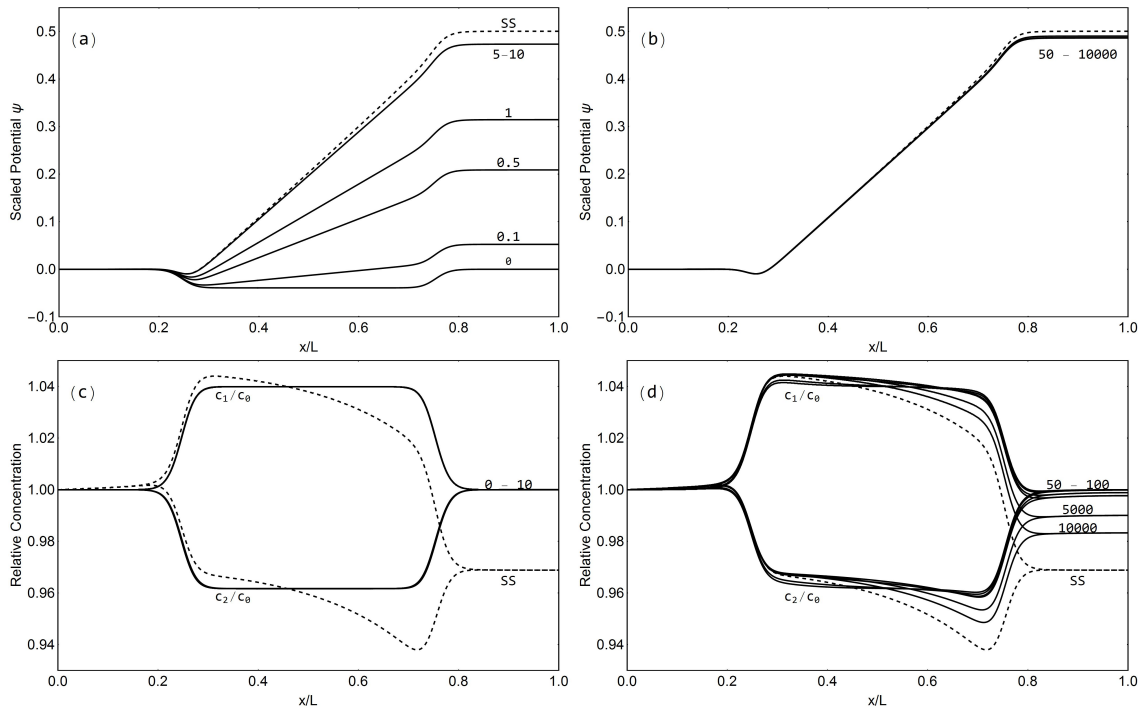

Figure 4.7: Time evolution of the scaled electric potential $\bar{\phi}$ and relative ion concentration profiles c_i/c_∞ along the channel axis. The scaled channel radius is $\kappa a = 5$ and the pressure gradient is 1×10^7 Pa/m. The graphs on the left show the electric potential and ion concentration directly after application of a pressure gradient ($\tau \leq 10$), while the graphs on the right show later times up to $\tau = 10.000$. Here, *SS* denoted the steady-state solution.

4.1.3 Pressure Driven and Electroosmostic Flow

Finally, we look at the effect of an applied external electric field on the exit reservoir. Now, apart from pressure driven flow, electrokinetic flow is also present. Moreover, the electric field can be chosen such that the generated electrokinetic flow works opposite to the pressure driven flow, leading to interesting axial velocity profiles.

4.1.3.1 Boundary Conditions

This general case of electroosmotic flow is treated as a variation on the steady-state analysis of the streaming potential. As such, all the boundary conditions of the first case are retained, except for the application of an electric field on the boundary FQ. This boundary condition is implemented in COMSOL by specifying the components of the displacement vector $\boldsymbol{D} = \varepsilon \boldsymbol{E}$. For the used values of $c_\infty = 1 \times 10^{-5}$ M and $\kappa = 1.038 \times 10^7$ m^{-1}, a scaled axial field of $E_0 = \bar{\boldsymbol{E}}_x \cdot \boldsymbol{i}_x = 0.01$ corresponds to an applied electric field of 2.67×10^3 V/m.

Boundary	Poisson	Nernst-Planck	Navier-Stokes
PQ	Axial symmetry	Axial symmetry	Axial symmetry
AB, EF	No charge	$\boldsymbol{n} \cdot \boldsymbol{J}_i = 0$	Full slip
BC, DE	No charge	$\boldsymbol{n} \cdot \boldsymbol{J}_i = 0$	No slip
CD	Constant charge density, ρ_c	$\boldsymbol{n} \cdot \boldsymbol{J}_i = 0$	No slip
AP	$\phi = 0$	$c_i = c_\infty$	Pressure p_0
FQ	$\boldsymbol{n} \cdot \boldsymbol{D} = \boldsymbol{n} \cdot \boldsymbol{D}_0$	$c_i = c_\infty$	Zero pressure

Table 4.5: A summary of the boundary conditions of the governing equations, used in the analysis of the combined pressure driven and electroosmostic flow.

4.1.3.2 Velocity Profiles for Electroomostic Flow

Fig. 4.8(a) shows the axial velocity $\boldsymbol{u}_x$, taken at the midsection ($\bar{x} = 0.5$) of the channel, in the case of pressure driven flow ($p = p_0$, $\bar{E}_0 = 0$), purely electrokinetic flow ($p = 0$, $\bar{E}_0 = 0.01$) and full electroosmotic flow ($p = p_0$, $\bar{E}_0 = 0.01$). The dashed line represents the sum of the axial velocity of the pressure driven and electroosmotic flow. As we can see, the linear superposition of the two pure flows deviates slightly from the numerical solution. While this indicates that the linear superposition is not exact, it does show that it is a decent approximation. This difference can be explained by looking at the pressure gradient (Fig. 4.8(a). In the case of combined pressure driven and electroosmotic flow, the resulting pressure gradient is vastly different from the superposition.

When the applied electric field E_0 is negative, the resulting electroosmotic flow counteracts the pressure driven flow. This is presented in Fig. 4.8b. For $\bar{E}_0 = -0.05$ we see that the parabolic velocity profile, found in the case of no applied electric field, is diminished. For $\bar{E}_0 = -0.01$ the fluid at the wall flows opposite to the fluid in the interior. When the elec-
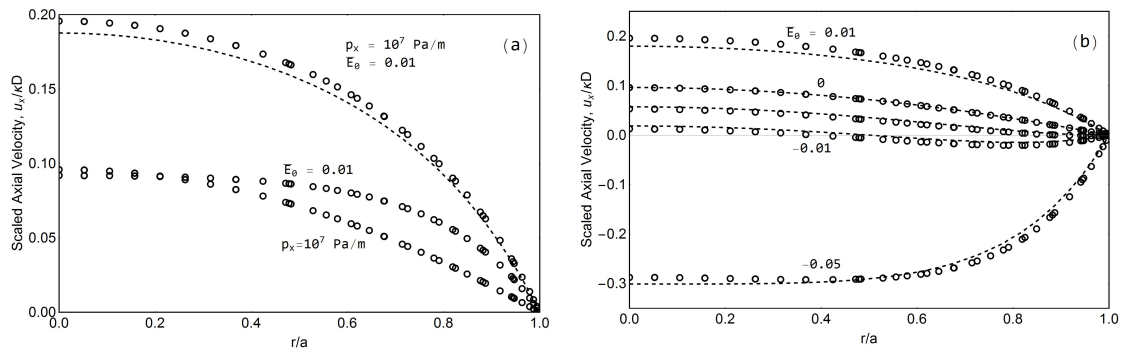
Figure 4.8: The steady-state scaled axial velocity profile, $u_x/\kappa D$, taken at the channel midsection $\bar{x} = 0.5$ for $\kappa a = 5$. (a) compares the sum of pressure driven and electroosmotic flow to the full electrokinetic flow profile, while (b) shows the axial velocity profile for several values of the applied electric field E_0.

tric field is increased further, electrokinetic flow takes over and the flow direction reverses completely. For all these situations, Eq. 2.20 describes the flow profile reasonably well.

4.2   Charge Regulating Model

Our basis is the model as described in section 4.1.2. This incorporates only pressure driven flow, but does account for ion rejection by the pore by specifying an outflowing boundary condition on FQ. Furthermore, we now replace the constant surface charge density at BC, CD and EF with the expression

$$\rho_c = -e \frac{\Gamma}{\frac{10^{-pK}}{c_2} + 1}.$$

(4.2)

Consequently, because the ion concentration varies greatly throughout the system, the surface charge will no longer be constant.

Fig. 4.9 shows the surface charge density profile of the side and channel wall, obtained by running the simulation for $\Gamma = 8$ 1/nm^2, commonly cited as the value for the total amount of sites for nonporous, fully hydrated sylica [15], and pK = 7.5, the value for silica obtained using a surface complexation model [13]. The pressure gradient took the values $1, 5$ and 10×10^7 Pa/m. Here, the scaled channel wall position α is determined by $\alpha = \bar{x} + \text{sign}(\bar{x}) \cdot \bar{r}$. In this figure, The domain $0.25 \leq x \leq 0.75$ represents the channel wall CD. The marked variations, occuring at the transition between the sidewall and channel wall, are due to the sharp corners in the geometry, which are relatively highly charged, and will be neglected in the following analysis.

We see that the surface charge density varies between -0.45 and -0.48 mC/m^2 and the dimensionless potential takes values between -2.1 and -1.5. Although significantly higher than the chosen surface charge density and dimensionless potential of section 4.1, these physical quantities are still well within the same order of magnitude.
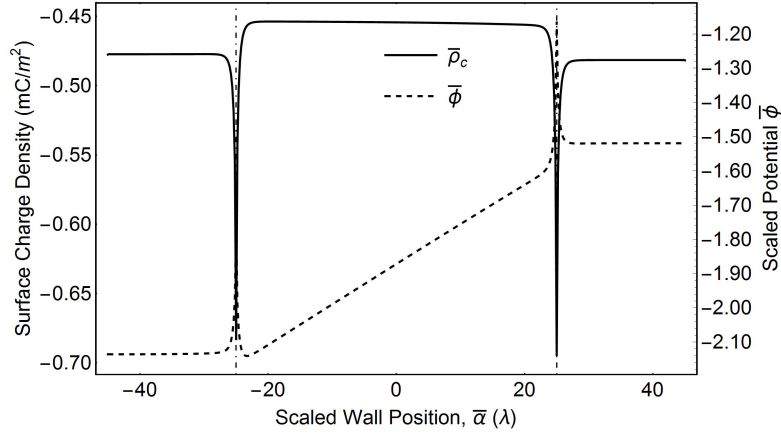

Figure 4.9: The value of the surface charge density and scaled electric potential at the channel and sidewalls. The scaled wall position α is determined by $\alpha = (\bar{x} + \text{sign}(\bar{x}) \cdot \bar{r})/\kappa$. The domain $-25 \leq x \leq 25$ represents the channel wall CD. The site density Γ was 8 1/(nm)^2 and pK was taken to be 7.5

4.2.1 Tuning the Surface Charge

Now we look at the effects of changing the parameters in our charge regulation model. These parameters, Γ and pK, can be physically manipulated by considering different solutions and channel materials. This effectively changes the equilibrium reaction 2.40, which leads to different surface charge density profiles. Fig. 4.10(a) shows the surface charge density on the channel and sidewalls for pK = 7, 8 and 9 and Γ = 8 and 12 1/nm². As we can see, the variation of pK has a significantly greater effect on the surface charge than changing the number of sites. This is due to the surface charge being determined by a small fraction of ionized sites 4.10(b).
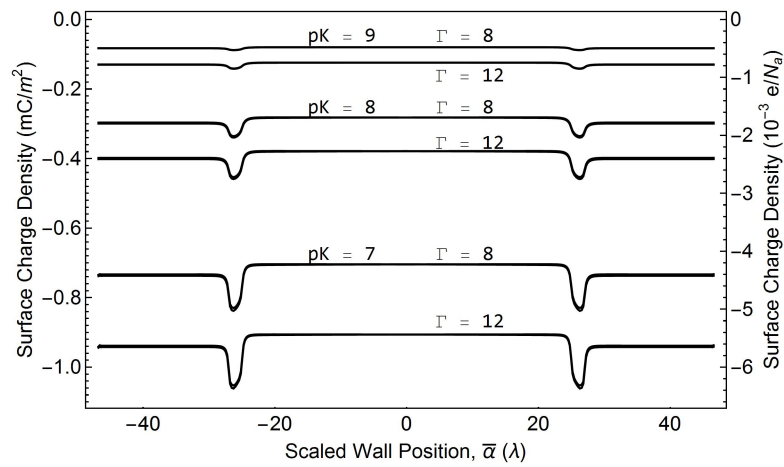

Figure 4.10: The value of the surface charge density taken at the channel wall and sidewalls for $pK = 8$ and 9 and $\Gamma = 8$ and 12. The scaled channel wall position α is determined by $\alpha = (\bar{x} + \text{sign}(\bar{x}) \cdot \bar{r})/\kappa$ The domain $-25 \leq x \leq 25$ represents the channel wall CD.

4.2.2 Comparison to the Non Charge Regulating Model

To get a better understanding of the consequences of the charge regulation boundary conditions, we will compare the results obtained using the charge regulating (CR) model against the constant surface charge density (non-CR) model. Throughout this section we set the total number density of sites to be 8 nm^{-2} as to match silica and pK = 8.3, resulting in a surface charge density ranging from -0.20 to -0.22 mC/m^2 for $\kappa a = 5$. This value of the surface charge density roughly matches the value used for the constant value in the previous section.

4.2.2.1 Pressure Driven Flow The application of a non-constant surface charge can greatly affects the electric double layer, by locally changing the width of the Stern layer. Moreover, when the channel radius is small we expect a greater depletion of ions in the channel. Due to the dependence of the surface charge density on the salt concentration in the channel, we expect that, for different channel widths, the surface charge will vary considerably. This will make a comparison convoluted.

We again analyse the streaming potential by demanding that the entrance and exit reservoirs have the same concentration c_∞. The pressure gradient was set to $p_x = 1 \times 10^7$ Pa/m and the scaled channel width κa was taken to be 6. Due to the relatively small difference in charge density between the side walls and the channel, we do not expect the potential to diverge greatly from the constant charge model. Fig. 4.11 depicts the potential and the axial electric field obtained used the CR and non CR model. The streaming potential is slightly diminshed, while the axial electric field, removed from the entrance and exit, is now constant. It is a well known fact that physical systems try to minimise their potential energy. Thus, the fact that the streaming potential is diminished speaks in favour of the CR model.
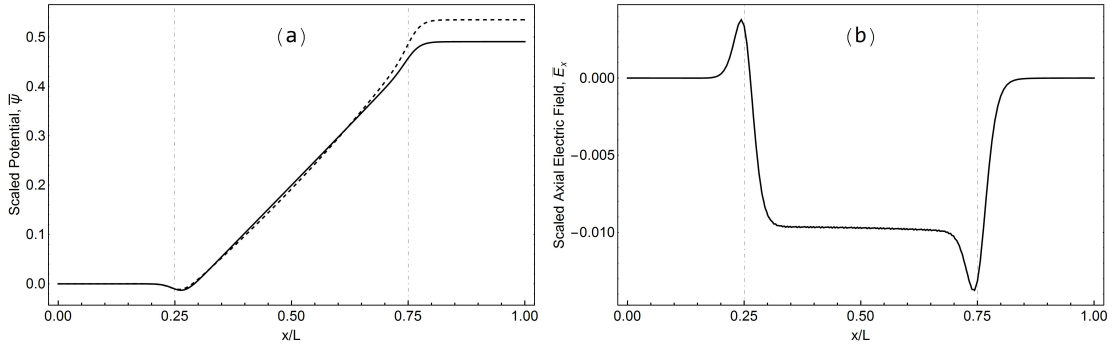

Figure 4.11: (a) The scaled electric potential $\bar{\phi}$ and the corresponding scaled axial electric field $\bar{E}_x$ (b) along the axis of symmetry obtained by solving the governing equations with the charge regulating boundary condition. The solid lines represents the the CR-model, while the dashed lines represent non-CR model. The simulation was run for $\kappa a = 5$ with a pressure gradient of 1×10^7 Pa/m, pK = 8.3 and $\Gamma = 8$ 1/(nm)^2. The vertical lines represent the entrance and exit of the channel.

Mirroring Section 4.1.1, we can compare the numerical solution against the 'analytical' ex-

pression 2.34. This is depicted in Fig. 4.12. We see that, for $L_c = 25\lambda_D$ and $50\lambda_D$, there is a considerable mismatch between the numerical values and the analytic expression. We attribute this to the fact that analytical expression assumes a constant axial electric field. For $L_c = 75\lambda_D$, the comparison seems to hold reasonably well.
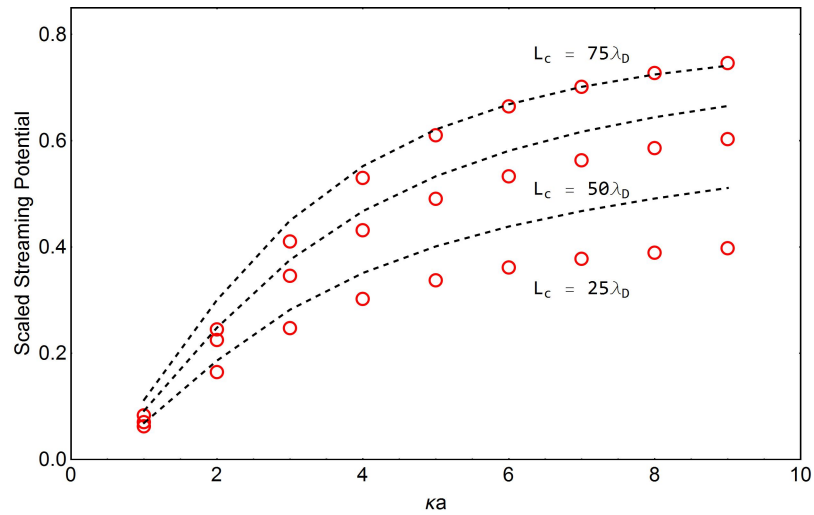

Figure 4.12: A comparison of the scaled streaming potential obtained from the numerical simulation and the prediction given by the calculation scheme of Masliyah and Bhattacharjee (2006) [22] for different values of the scaled channel radius κa. Here, pK is 8.3 and the density of sites Γ is 8 1/nm^2.

29

4.2.2.2 Time Evolution
In Section 4.1.2 we explored the time evolution of electric potential and ion concentration profiles. We concluded that the electric potential has a rapid buildup, whereas the ion concentration takes significantly longer to reach its steady state value. We now look at the effect of our charge regulating boundary condition on this time evolution. Just like in Section 4.1.2, the output of the simulation was stored for various values of the scaled time $\tau = \kappa^2 D t$. The initial state ($\tau = 0$) was determined by solving the model without an applied pressure gradient. The simulation was run for $\kappa a = 5$ and $p_x = 1 \times 10^7$ Pa/m.

The left side of Fig. 4.13 shows the electric potential and ion concentration profiles directly after the application of the pressure ($\tau \leq 10$, i.e. $t = 0.1$ ms), whereas the right figure shows later times. Again we see that the electric potential sets in rapidly, whereas the ion concentration takes significantly longer to react. We conclude that the altered boundary condition does not seem to affect the time evolution of the electric potential and ion concentration profiles.
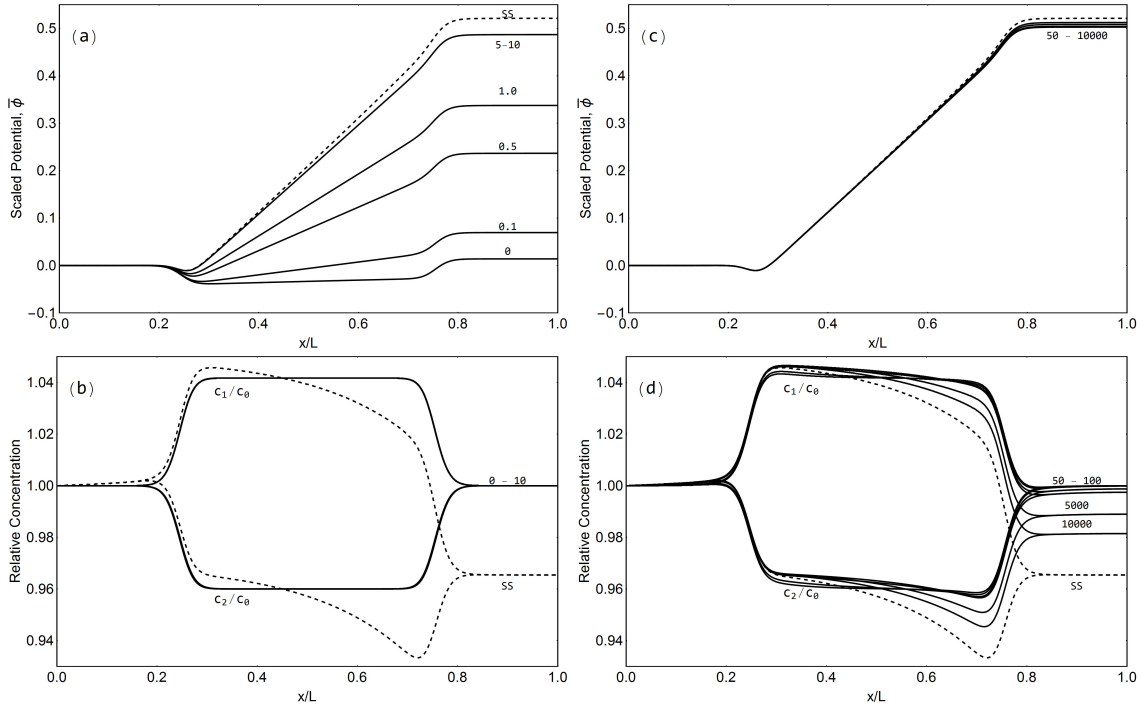

Figure 4.13: Development of the scaled electric potential $\bar{\phi}$ and relative ion concentration profiles c_i/c_∞ along the channel axis. The scaled channel radius is $\kappa a = 5$ and the pressure gradient is 1×10^7 Pa/m. The graphs on the left show the electric potential and ion concentration directly after application of a pressure gradient ($\tau \leq 10$), while the graphs on the right show later times up to $\tau = 10.000$. Here, *SS* denoted the steady-state solution.

4.2.3 Effect of an External Electric Field

Finally we look at the effect of applying an external electric field on the boundary FQ. Apart from exhibiting a force on the fluid, we also expect the channel surface charge to react to the electric field and redistribute accordingly. Fig. 4.14 shows the surface charge density for $\bar{E}_0 = -0.01, 0$ and 0.01, where $x \leq 25$ and $x \geq 75$ represent the sidewalls BC and DE, and $25 \leq x \leq 75$ represents the channel wall CD. As we can see, instead of the charge being constant on the channel wall, it now appears to be increasing linearly along the wall.
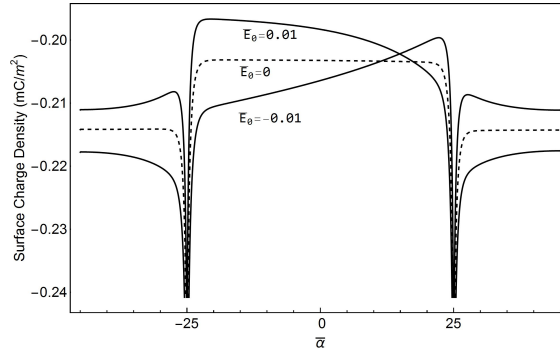

Figure 4.14: The surface charge density at the channel wall and sidewalls for different values of the applied electric field E_0. The scaled channel wall position α is determined by $\alpha = (\bar{x} + \text{sign}(\bar{x}) \cdot \bar{r})/\kappa$ The domain $-25 \leq x \leq 25$ represents the channel wall CD. The site density Γ was 8 $1/(nm)^2$ and pK was taken to be 8.3.

We again compare the axial velocity profile at the midsection of the channel to the analytical expression Eq. 4.1. For low field strength, the comparison between the numerical values and the anaytic expression seems to hold reasonably well. However, when the electroosmotic flow starts to dominate the electrokinetic flow, a far lower axial velocity is obtained. We attribute this to the strong electric field having a greater effect on the surface charge.
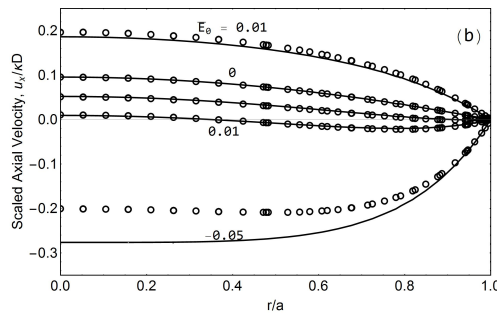

Figure 4.15: The steady-state scaled axial velocity profile, $u_x/\kappa D$, taken at the channel midsection $\bar{x} = 0.5$ for $\kappa a = 5$. (a) compares the sum of pressure driven and electroosmotic flow to the full electrokinetic flow profile, while (b) shows the axial velocity profile for several values of the applied electric field E_0.

31

5   Conclusion and Outlook

We have developed a numerical model that describes the ion transport and fluid flow through a charged microchannel under the application of a pressure gradiënt and an external electric field. Moreover, we succcesfully replaced the conventional constant surface charge boundary condition on the channel in favour of a surface charge that is determined through a simple charge regulation scheme.

Due to the altered boundary condition, the surface charge on the channel wall and sidewalls redistributes, resulting in a lower streaming potential and a constant axial electric field at the channel wall. Just as in the constant surface charge model, the electric potential reaches near equilibrium within the first 0.1 ms, while the axial ion concentration profiles take far longer to reach their equilibrium values. When an external electric field is applied, the surface charge on the boundary reacts accordingly and redistributes. When the applied electric field is weak ($E_0 \leq 0.01$) the axial velocity profiles are similar to the values found by employing the constant charge model. However, when the electroosmotic flow starts to dominate the electrokinetic flow, a far lower axial velocity is predicted. Our explanation for this is the redistribution of the channel surface charge under the applied electric field which causes a weaker axial electric field inside the channel.

Further insights may be gained by considering smaller channels and looking at the effect of overlapping electric double layers. Furthermore, more complex charge regulation mechanisms, such as multiple chemical reactions, can be considered.

6 Acknowledgements

References

[1] F. Baldessari. Electrokinetics in nanochannels: Part i. electric double layer overlap and channel-to-well equilibrium. *Journal of Colloid and Interface Science*, 325(2):526 – 538, 2008.

[2] J.-L. Barrat and L. Bocquet. Large slip effect at a nonwetting fluid-solid interface. *Physical review letters*, 82(23):4671, 1999.

[3] K.-J. Bathe. *Finite element procedures*. Klaus-Jurgen Bathe, 2006.

[4] T. P. Burg and S. R. Manalis. Suspended microchannel resonators for biomolecular detection. *Applied Physics Letters*, 83(13):2698–2700, 2003.

[5] H. Daiguji, P. Yang, and A. Majumdar. Ion transport in nanofluidic channels. *Nano Letters*, 4(1):137–142, 2004.

[6] H. Daiguji, P. Yang, and A. Majumdar. Ion transport in nanofluidic channels. *Nano Letters*, 4(1):137–142, 2004.

[7] H. Daiguji, P. Yang, A. J. Szeri, and A. Majumdar. Electrochemomechanical energy conversion in nanofluidic channels. *Nano letters*, 4(12):2315–2321, 2004.

[8] W. de Lint, P. Biesheuvel, and H. Verweij. Application of the charge regulation model to transport of ions through hydrophilic membranes: One-dimensional transport model for narrow pores (nanofiltration). *Journal of Colloid and Interface Science*, 251(1):131 – 142, 2002.

[9] D. H. Everett. *Basic Principles of Colloid Science*. Royal Society of Chemistry, London, 1988.

[10] H. Helmholtz. Ueber einige gesetze der vertheilung elektrischer strome in korperlichen leitern mit anwendung auf die thierisch-elektrischen versuche. *Annalen der Physik*, 165(6):211 – 233, 1853.

[11] P. C. Hiemenz and R. Rajagopalan. *Principles of Colloid and Surface Chemistry, 3rd ed.* Marcell Dekker, New York, 1997.

[12] T. Hiemstra and W. V. Riemsdijk. A surface structural approach to ion adsorption: The charge distribution (cd) model. *Journal of Colloid and Interface Science*, 179(2):488 – 508, 1996.

[13] T. Hiemstra, W. Van Riemsdijk, and G. Bolt. Multisite proton adsorption modeling at the solid/solution interface of (hydr) oxides: A new approach: I. model description and evaluation of intrinsic reaction constants. *Journal of colloid and interface science*, 133(1):91–104, 1989.

[14] R. J. Hunter. *Zeta Potential in Colloid Science*. Academic Press, 1981.

[15] R. K. Iler et al. The chemistry of silica, 1979.

[16] Y. J and D. Kwok. Effect of liquid slip in electrokinetic parallel-plate microchannel flow. *Journal of Colloid and Interface Science*, 260(1):225 – 233, 2003.

[17] H. J. Keh and H. C. Tseng. Transient electrokinetic flow in fine capillaries. *Journal of colloid and Interface Science*, 242(2):450–459, 2001.

[18] S. J. Kim, S. H. Ko, K. H. Kang, and J. Han. Direct seawater desalination by ion concentration polarization. *Nature Nanotechnology*, 5(4):297–301, 2010.

[19] E. Lauga, M. Brenner, and H. Stone. Microfluidics: the no-slip boundary condition. In *Springer handbook of experimental fluid mechanics*, pages 1219–1240. Springer Berlin Heidelberg, 2007.

[20] A. Mansouri, C. Scheuerman, S. Bhattacharjee, D. Y. Kwok, and L. W. Kostiuk. Transient streaming potential in a finite length microchannel. *Journal of Colloid and Interface Science*, 292(2):567 – 580, 2005.

[21] T. Markovich, D. Andelman, and R. Podgornik. Charge regulation: A generalized boundary condition? *EPL (Europhysics Letters)*, 113(2):26004, 2016.

[22] J. Masliyah and S. Bhattacharjee. *Electrokinetic and colloid transport phenomena*. Wiley Interscience, 2006.

[23] J. Maxwell. On stresses in rarefied gases arising from inequalities of temperature. *Phil. Trans. R. Soc. Lond.*, 170:231256, 1879.

[24] R. M. McCormick, R. J. Nelson, M. G. Alonso-Amigo, D. J. Benvegnu, and H. H. Hooper. Microchannel electrophoretic separations of dna in injection-molded plastic substrates. *Analytical Chemistry*, 69(14):2626–2630, 1997.

[25] F. Morrison. Transient electrophoresis of a dielectric sphere. *Journal of Colloid and Interface Science*, 29(4):687–691, 1969.

[26] C. Navier. Memoire sur les lois du mouvement des fluides. *Memoires de l'Academie Royale des Sciences de l'Institut de France*, 6:389440, 1823.

[27] H. Park, J. Lee, and T. Kim. Comparison of the nernstplanck model and the poisson-boltzmann model for electroosmotic flows in microchannels. *Journal of Colloid and Interface Science*, 315(2):731 – 739, 2007.

[28] T. Postler, Z. Slouka, M. Svoboda, M. Pribyl, and D. Snita. Parametrical studies of electroosmotic transport characteristics in submicrometer channels. *Journal of Colloid and Interface Science*, 320(1):321 – 332, 2008.

[29] R. F. Probstein. *Physicochemical Hydrodynamics, An Introduction*. Wiley Interscience, New York, 2003.

[30] C. L. Rice and R. Whitehead. Electrokinetic flow in a narrow cylindrical capillary. *Journal of Physical Chemistry*, 69:40174024, 1965.

[31] E. Ruckenstein and P. Rajora. On the no-slip boundary condition of hydrodynamics. *Journal of colloid and interface science*, 96(2):488–491, 1983.

[32] V. D. Sobolev, T. A. Vorobyova, and O. A. Kiseleva. Determination of surface potential of hollow fiber membranes by streaming potential method. *Petroleum Chemistry*, 54(8):612–616, 2014.

[33] J. Sonnefeld. Surface charge density on spherical silica particles in aqueous alkali chloride solutions. *Colloid and Polymer Science*, 273(10):932–938, 1995.

[34] D. Stein, M. Kruithof, and C. Dekker. Surface-charge-governed ion transport in nanofluidic channels. *Phys. Rev. Lett.*, 93:035901, Jul 2004.

[35] A. Sverjensky, D and N. Sahai. Theoretical prediction of single-site surface-protonation equilibrium constants for oxides and silicates in water. *Geochimica et Cosmochimica Acta*, 60(20):3773 – 3797, 1996.

[36] D. Sverjensky. Prediction of surface charge on oxides in salt solutions: Revisions for 1:1 (m+l) electrolytes. *Geochimica et Cosmochimica Acta*, 69(2):225 – 257, 2005.

[37] J. Takagi, M. Yamada, M. Yasuda, and M. Seki. Continuous particle separation in a microchannel having asymmetrically arranged multiple branches. *Lab on a Chip*, 5(7):778–784, 2005.

[38] V. Tandon and B. Kirby. Zeta potential and electroosmotic mobility in microfluidic devices fabricated from hydrophobic polymers: 2. slip and interfacial water structure. *ELECTROPHORESIS*, 29(5):1102–1114, 2008.

[39] D. C. Tretheway and C. D. Meinhart. Apparent fluid slip at hydrophobic microchannel walls. *Physics of Fluids (1994-present)*, 14(3):L9–L12, 2002.

[40] D. van der Heyden, D. Bonthuis, D. Stein, C. Meyer, and C. Dekker. Power generation by pressure-driven transport of ions in nanofluidic channels. *Nano Letters*, 7(4):1022–1025, 2007.

[41] F. van der Heyden, D. Stein, and C. Dekker. Streaming currents in a single nanofluidic channel. *Phys. Rev. Lett.*, 95:116104, Sep 2005.

[42] J. Westall and H. Hohl. A comparison of electrostatic models for the oxide/solution interface. *Advances in Colloid and Interface Science*, 12(4):265 – 294, 1980.

[43] R. Yang, L. Fu, and C. Hwang. Electroosmotic entry flow in a microchannel. *Journal of Colloid and Interface Science*, 244(1):173 – 179, 2001.

[44] C. Yong-Seok and K. Sung-Jin. Electrokinetic flow-induced currents in silica nanofluidic channels. *Journal of Colloid and Interface Science*, 333(2):672 – 678, 2009.

[45] J. Zhu, Z. Taylor, and O. Zienkiewicz. *The finite element method: its basis and fundamentals*. Elsevier, 2013.

[46] Y. Zhu and S. Granick. Rate-dependent slip of newtonian liquid at smooth surfaces. *Physical review letters*, 87(9):096105, 2001.